Acta of Bioengineering and Biomechanics
Vol. 16, No. 4, 2014

Original paper
DOI: 10.5277/ABB-00029-2014-05

Numerical investigations of pulsatile flow in stenosed artery

ARINDAM BIT[1]*, HIMADRI CHATTOPADHYAY[2]

[1] Department of Biomedical Engineering, National Institute of Technology, Raipur, India.
[2] School of Bioscience and Engineering, and Department of Mechanical Engineering, Jadavpur University, India.

Purpose: Abnormalities in blood vessels by virtue of complex blood flow dynamics is being supported by non-Newtonian behavior of blood. Thus it becomes a focus of research to most of the researchers. Additionally, consideration of real life patient specific model of vessel as well as patient specific inlet flow boundary condition implementation was limited in literature. Thus a thorough implementation of these considerations was done here.

Method: In this work, a numerical investigation of hemodynamic flow in stenosed artery has been carried out with realistic pulsating profile at the inlet. Flow has been considered to be laminar due to arresting condition of cardiovascular state of the subject. Two non-Newtonian rheological models namely, Power Law viscosity model and Quemada viscosity model have been used. Two different patient-specific pulsatile profiles are considered at the inlet of a long stenosed artery with varying degree of stenoses from 25% to 80%.

Results: Transient form of Navier-Stokes equation is solved in an axi-symmetric domain to calculate the detailed flow structure of the flow field. From the simulation data, temporal and time averaged wall shear stress, oscillatory shear index and pressure drop are calculated.

Conclusions: The results demonstrate that oscillatory shear index and wall shear stresses are extensively governed by the degree of stenoses. The position and movement of recirculation bubbles are found to vary with flow Reynolds number.

Key words: *non-Newtonian, pulsatile, hemodynamic, stenoses, oscillatory shear index, Reynolds number*

1. Introduction

For the past few decades cardiovascular diseases have become the third largest cause of mortality across the globe, where stenoses is of special concern. This leads several research communities investigating the above problem with due considerations from the transport process angle. Hemodynamic plays a significant role in understanding the arterial wall thickening process as well as the effect of stenoses on the flow structure. The transport process in stenotic blood vessels deals with different complex issues such as the pulsating nature of flow field and an appropriate rheological description of the fluid.

A detailed study of the state of art about the stenoses and physics contributing to the phenomena reveals some of the important contribution made by several researchers across the world. Ai et al. [1] used interfacing of MEMS thermal sensor with high frequency pulse wave Doppler ultrasound for the study of actual physiological flow profile of the problem. Simultaneously, Beratilis et al. [2] had investigated turbulent behaviour of hemodynamic through diseased vessel. Drikakis et al. [3] investigated the blood flow behavior in reconstructive surgery considering the simplest form of pulsatile flow, whereas few studies had also been carried out considering the real geometry of stenosed blood vessel [4]. According to Johnston et al. [5] non-Newtonian effects of blood viscosity model could become important while studying transient flows in complex geometries, like arch of aorta, bifurcation.

In most of the studies, attempts have been made either to realize the exact geometry of the stenosed

* Corresponding author: Arindam Bit, Department of Biomedical Engineering, National Institute of Technology, Raipur, Pin 492010, India. Tel: 919098033297, e-mail: ab.mbme@gmail.com

Received: April 23rd, 2014
Accepted for publication: April 24th, 2014

wall, or pulsatile flows at inlet. Earlier, Jinyou and Yang [6] had used CT scan data for realizing the geometry of the problem. Li and Kleinstreuer [7] used Quemada viscosity model of blood with the FSI effect on sac blood pressure and wall pressure while performing a comparison test between numerical and experimental studies. Blood flow phenomenon through stenosed vessel is not limited to laminar flow. It often goes in the regime of transition to turbulence in critical conditions. Thereby studies on the turbulent behavior of the blood flow through stenosed vessel have been done extensively for a decade by several researchers [2], [8], [9] and [10]. Neofytou and Drikakis [9] analyzed the problem by considering three different viscosity models (Casson, Power Law and Quemada) for comparative study of the blood flow through stenoses. Several researchers used perturbation theory for solving the same problem considering the pulsatile nature of blood flow as sine wave and emphasized the role of Womersley number on the properties of flow behaviour [11] and [12]. Rigid wall boundary had replaced the realistic elastic nature of blood vessels throughout decades by several researchers [13] and [14]. Womersley et al. [14] had developed Womersley parameter ($\alpha = R \times (\omega/\nu)^{1/2}$) which issued in the transform developed in Stoke's second problem, in which flow is induced by an oscillating flat plate. Mostly, walls of the blood vessels are considered as rigid walls for the simplicity of problem.

The above survey reflects that despite the existence of a comprehensive work on the subject, comparative assessment of the non-Newtonian rheological models on the dynamics of flow due to realistic pulsatile flow at the inlet of the vessel is scarec. In this work, a numerical investigation of the transport phenomena in stenosed blood vessel considering 2-D axi-symmetric geometry has been done for performance assessment of non-Newtonian viscosity models (Power Law model, and Quemada model), with consideration of realistic pulsation at the inlet of the vessel. The degree of stenoses is varied from 25% to 80%, and they are considered to be function of the upstream length of stenoses and depth of stenoses, driving the geometry of stenoses more approximate to reality. Two input flow profiles (one from literature and another from patient specific data) at two separate flow levels for each case are considered purely to be physiological pulses of pressure driven mass flow rate, making the study most appropriate with the input boundary condition. Cumulative effects of all the above parameters are studied for different frequencies of WSS, and OSI.

2. Materials and methods

The axi-symmetric computational domain is given in Fig. 1, and the stenoses profile is defined by Neofytou and Drikakis [9] as follows

$$y = 0,\ y = 1,\ \forall x \in [0,7] \cup [11.6,40], \tag{1}$$

$$y = 0,\ y = 1 - (a - R + \sqrt{R^2 - [b/2 - (x - L_u)]^2}), \tag{2}$$

where $R = \dfrac{[a^2 + (b/2)^2]}{2a}$, and a = 0.56, b = 4.66. a and b are functional depth of stenoses and length of stenoses, respectively; L_u, L_d, and l represent upstream length of vessel, downstream length of vessel, and length scale, respectively; H represents distance between the symmetric axis and the wall. The blockage of the vessel, i.e., the degree of stenoses is defined as the ratio of maximum height of stenosed part a to the vessel inner radius R.

Localised pressure deflections leading to compressibility of fluid due to fluid structure interactions are neglected, and incompressibility property has been considered for the simplicity of the model. This reduces the mass conservation continuity equation, which is given by equation (3) as

$$\frac{1}{r}\frac{\partial}{\partial r}(rv) + \frac{\partial}{\partial x}(u) = 0 \tag{3}$$

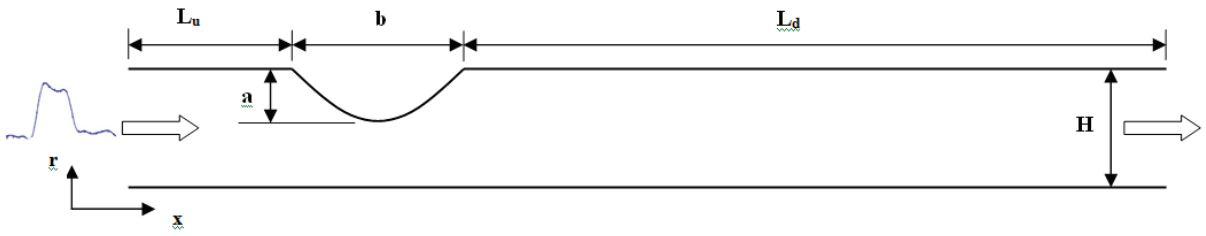

Fig. 1. Stenosed blood vessel geometry definition

where u and v represent non-dimensional velocity components in x and y directions, respectively. Similarly the conservation of momentum equation along the axis of symmetry as well as along the radial direction consists of a transient term, convective term, a negative pressure term, and diffusion term, and can be represented by equations (4) and (5) as:

- axial momentum equation

$$\frac{\partial u}{\partial t}+\frac{1}{r}\frac{\partial}{\partial r}(ruv)+\frac{\partial}{\partial x}(u^2) = -\frac{1}{\rho}\frac{\partial p}{\partial x}+\frac{1}{r}\frac{\partial}{\partial r}\left(\frac{\mu_{\text{app}}}{\rho}r\left(\frac{\partial u}{\partial r}+\frac{\partial v}{\partial x}\right)\right)+\frac{\partial}{\partial x}\left[\frac{2\mu_{\text{app}}}{\rho}\frac{\partial u}{\partial x}\right] \tag{4}$$

- r – momentum equation

$$\frac{\partial v}{\partial t}+\frac{1}{r}\frac{\partial}{\partial r}(rv^2)+\frac{\partial}{\partial x}(uv) = -\frac{1}{\rho}\frac{\partial p}{\partial r}+\frac{1}{r}\frac{\partial}{\partial r}\left(\frac{2\mu_{\text{app}}}{\rho}r\frac{\partial v}{\partial r}\right) -\frac{2\mu_{\text{app}}}{\rho}\frac{v}{r^2}+\frac{\partial}{\partial x}\left[\frac{\mu_{\text{app}}}{\rho}\left(\frac{\partial u}{\partial r}+\frac{\partial v}{\partial x}\right)\right] \tag{5}$$

where μ_{app} and ρ are apparent viscosity and density of blood, respectively. The wall of the stenosed blood vessel has been considered as rigid wall [15]–[17], implementing a no slip boundary condition at the wall, while a zero gauge output pressure has been considered at the output of the vessel due to the presence of the whole system (stenosed blood vessel) in the submerged body fluid. Input mass flow rate have been considered the most realistic transient physiological flow profiles of different physiological states, and different Re numbers, as given in Table 1. Two physiological input velocity profiles are given in Fig. 2(a) and (b), which have been described later. The no-slip boundary condition can be expressed mathematically as $u = v = 0$ on the walls and the pressure outlet condition can be expressed as the gauge pressure $p = 0$ at the outlet. The pulsating inlet profiles are discussed in the following section in equation form.

Table 1. Mean velocities and corresponding Reynolds numbers of inlet profiles used

Inlet velocity profile type	Mean velocity (m/s)	Reynolds number	
1	0.15	1060	Re I
2	0.0977	690	
1 × 2	0.30	2120	Re II
2 × 2	0.1954	1380	

Considering the blood viscosity as non-Newtonian, Power Law model proposed by Walburn and Schneck [15], hematocrit and total protein minus albumin was taken into account. It is known as Power law model, also referred to as "Best three variable model". It is represented by the system of equations (6) and (7).

$$\bar{\tau} = k\left|\bar{\gamma}\right|^{n-1}\bar{\gamma} \tag{6}$$

and

$$\mu(\left|\bar{\gamma}\right|^{*}) = k\frac{U_{\infty}^{n-1}}{l^{n-1}}\left|\bar{\gamma}\right|^{*n-1} \tag{7}$$

where τ and γ are the shear stress and shear strain, respectively. For normal blood samples the parameters are k (consistency index) $=14.67 \times 10^{-3}$ Pa s, and n (flow behaviour index) = 0.7755 as described by Ku et al. [16]. If $n > 1$, the fluid is known as shear-thickening, while if $n < 1$ it is known as the shear thinning fluid. The characteristic parameter for a Power-Law-model-based flow is Re_{PL} (Reynolds number associated with Power Law Model).

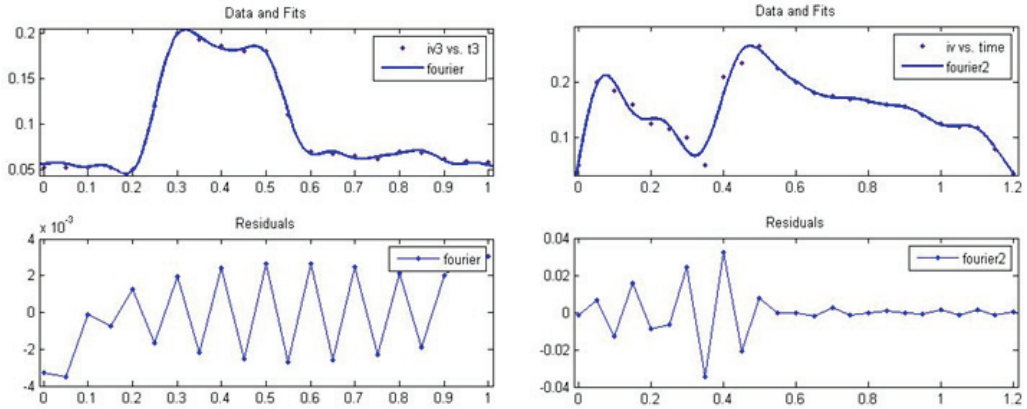

(a) Type 1 velocity profile (b) Type 2 velocity profile

Fig. 2. Two different inlet velocity profiles

Further considering the viscosity of concentrated disperse system, Quemada [17] proposed a model based on shear rate and haematocrit. The system of equations of shear stress and effective viscosity in tensorial form and dimensionless form are as follows:

$$\bar{\tau} = \mu_F \left(1 - \frac{1}{2} \frac{k_0 + k_\infty \sqrt{|\bar{\gamma}|/\gamma_c}}{1 + \sqrt{|\bar{\gamma}|/\gamma_c}} \varphi \right)^{-2} \bar{\gamma} \tag{8}$$

and

$$\mu(|\bar{\gamma}|^*) = \mu_F \left(1 - \frac{1}{2} \frac{k_0 + k_\infty \sqrt{|\bar{\gamma}|^*/\gamma_c^*}}{1 + \sqrt{|\bar{\gamma}|^*/\gamma_c^*}} \varphi \right)^{-2} \tag{9}$$

where $\gamma_c^* = \dfrac{\gamma_c}{U_\infty / l}$ is the reference shear rate, and the parameters are given as $\mu_F = 1.2 \times 10^{-3}$ Pa.s is the viscosity of plasma (suspending medium), and for haematocrit $\varphi = 0.45$, the values of the parameters are $\gamma_c = 1.88\ s^{-1}$, $k_\infty = 2.07$ and $k_0 = 4.33$. The characteristic parameters for a Quemada-model-based flow are Re_{QU} (Reynolds number associated with Quemada model) and γ_c^*.

Velocity profiles considered are curve-fitted for transient simulation, as depicted in Fig. 2. Blood flow through stenosed ascending aorta of a ventricular fibrillating patient at Podder Hospital, Kolkata was measured using Ultrasonic Doppler Velocity-meter, and is represented as Type 1 inlet velocity profile, realized as Fourier function, and it is given by equation 10, having R-square = 0.9532, and RMSE = 0.02362.

$$\begin{aligned} u(t) = {} & 0.1223 + a1 \times \cos(\omega t) + b1 \times \sin(\omega t) \\ & + a2 \times \cos(2\omega t) + b2 \times \sin(2\omega t) + a3 \times \cos(3\omega t) \\ & + b3 \times \sin(3\omega t) + a4 \times \cos(4\omega t) + b4 \times \sin(4\omega t) \\ & + a5 \times \cos(5\omega t) + b5 \times \sin(5\omega t) + a6 \times \cos(6\omega t) \\ & + b6 \times \sin(6\omega t) + a7 \times \cos(7\omega t) + b7 \times \sin(7\omega t) \\ & + a8 \times \cos(8\omega t) + b8 \times \sin(8\omega t) \end{aligned} \tag{10}$$

where ω = 4.436, and the coefficients a's and b's are defined in Table 2. The above profile is of Re = 1060. For Re = 2120, the coefficients would be doubled.

Table 2. Parameters for velocity profile I

Type 1 waveform			
a1	–0.0808	b1	0.05008
a2	–0.01045	b2	0.0276
a3	0.01747	b3	0.05915
a4	–0.01034	b4	0.0504
a5	0.0002387	b5	0.01144
a6	0.01345	b6	0.01187
a7	0.002937	b7	0.01849
a8	0.003077	b8	0.009732

In the other case, the variation of the cross-sectional average velocity at the model inlet as described by Tan et al. [18] is realized by Fourier function, with R-square = 0.9981, and RMSE = 0.006317. Type 2 inlet velocity profile is given by equation (11).

$$\begin{aligned} u(t) = {} & 0.1006 + a1 \times \cos(\omega t) + b1 \times \sin(\omega t) \\ & + a2 \times \cos(2\omega t) + b2 \times \sin(2\omega t) + a3 \times \cos(3\omega t) \\ & + b3 \times \sin(3\omega t) + a4 \times \cos(4\omega t) + b4 \times \sin(4\omega t) \\ & + a5 \times \cos(5\omega t) + b5 \times \sin(5\omega t) + a6 \times \cos(6\omega t) \\ & + b6 \times \sin(6\omega t) + a7 \times \cos(7\omega t) + b7 \times \sin(7\omega t) \\ & + a8 \times \cos(8\omega t) + b8 \times \sin(8\omega t) \end{aligned} \tag{11}$$

where ω = 6.709, and the coefficients a's and b's are tabulated in Table 3. Here again, coefficients would be double when Re is made double. Table 1 shows the average velocity values and corresponding Reynolds number for the two different inlet profiles. It is observed that the value of Re is within the range of 690–2120, implying a laminar flow regime.

Table 3. Parameters for velocity profile II

Type 2 waveform			
a1	–0.06001	b1	0.02598
a2	0.01797	b2	–0.03354
a3	0.004013	b3	0.0036
a4	0.0002017	b4	0.0123
a5	–0.01081	b5	–0.008332
a6	0.004275	b6	0.0008295
a7	0.002519	b7	0.0002386
a8	–0.002491	b8	0.002568

Simulations were performed with a mesh size of 150 × 30. Before selecting the final mesh, a rigorous grid independence check has been carried out with three levels of grid sizes at 120 × 25, 150×30 and 180 × 35 cells. The grid independent extrapolated values of velocity components were evaluated at several locations considering grid independence study, as

mentioned below. The values of velocity components evaluated from the present mesh differed by less than 1% from the extrapolated value, and accordingly the present mesh was adopted for further analysis.

Richardson extrapolation is used to calculate a higher-order estimate of the flow fields from a series of lower-order discrete values ($f_1, f_2, ..., f_n$). The value estimated from the Richardson extrapolation is the value that would result if the cell grid size tended to zero, ($h \to 0$). The extrapolation is made from the results of at least two different grid solutions. Roache [19] generalized Richardson extrapolation by introducing the p-th-order methods,

$$f_{\text{exact}} \approx f_1 + \left[\frac{(f_1 - f_2)}{(r^p - 1)}\right], \tag{12}$$

In this study, the grid refinement ratio r, is mean refinement ratio r_{mean} of r_1 and r_2.

$$r = r_{\text{mean}} = \left(\frac{r_a + r_b}{2}\right) = \left(\frac{2.5 + 1.4}{2}\right) = 1.95 \tag{13}$$

where

$$r_a = \frac{\Delta_1}{\Delta_2} = \frac{0.05}{0.02} = 2.5 \quad \text{and} \quad r_b = \frac{\Delta_2}{\Delta_3} = \frac{0.02}{0.014} = 1.4\,. \tag{14}$$

Here, subscripts 1, 2, and 3 represent cases of study with different grid sizes. From equation (12), the extrapolated value is varied by different choice of the order p. According to Stern et al. [30] the order of accuracy can be estimated by using equation (15),

$$p = \frac{\ln(\varepsilon_{32} / \varepsilon_{21})}{\ln(r)}, \tag{15}$$

where

$$\varepsilon_{i+1,i} = f_{i+1} - f_i\,. \tag{16}$$

To evaluate the extrapolated value from these solutions, the convergence conditions of the system must be first determined. The possible convergence conditions are:

1. Monotonic convergence: $0 < R < 1$;
2. Oscillatory convergence: $R < 0$;
3. Divergence: $R > 1$;

where R is the convergence ratio and it is determined by equation (17):

$$R = \frac{\varepsilon_{21}}{\varepsilon_{32}}. \tag{17}$$

Table 4 summarizes the order of accuracy for prestenoses axial mean velocity ($V_{\text{axial(mean)}}$), and Absolute Wall Shear Stress (WSS_{Abs}) from the simulation results on three grids. The convergence conditions for $V_{\text{axial(mean)}}$ and WSS_{Abs} are monotonic. The Grid Convergence Index (GCI) provides a uniform measure of convergence for grid refinement study [20]. It is based on estimated fractional error derived from generalization of Richardson extrapolation. For fine grid solution, GCI can be represented by equation (18),

$$\text{GCI}_{i+1,i} = F_s \frac{|\,\varepsilon_{i+1,i}\,|}{f_i(r^p - 1)}\,. \tag{18}$$

The safety factor (F_s) selected for this study is considered to be 1.25.

Table 4. Order of accuracy and grid convergence index for 2 variables

	ε_{32}	ε_{21}	R	p	GCI_{32} (%)	GCI_{21} (%)
$V_{\text{axial(mean)}}$	0.0035	0.0018	0.514	0.9957	4.7126	2.48688
WSS_{Abs}	0.0159	0.0077	0.484	1.0857	4.2409	2.09036

As listed in Table 4, there is a reducted GCI value for the successive grid refinements ($\text{GCI}_{21} < \text{GCI}_{32}$) about each of the two variables. The GCI for finer grid (GCI_{21}) is relatively low if compared to the coarser grid (GCI_{32}), indicating that the dependence of the numerical simulation on the cell size has been reduced. Additionally, as the GCI reduction from the coarser grid to the finer grid is relatively high, the grid independent solution can be said to have been nearly achieved. Further refinement of the grid will not give much change in the simulation results. For variable $V_{\text{axial(mean)}}$, the extrapolated value is only slightly lower than the finer grid solution ($h/D = 0.002$) and it is in the range of the finer grid GCI as shown in the Fig. 3. Similar behaviour is observed for the variable of WSS_{Abs}. Therefore, it is shown that the solution has converged with the refinement from coarser grid to the finer grid.

The fluid mechanical equations were solved using the SIMPLE formulation [21]. In order to achieve higher accuracy, QUICK scheme is used to discrete the convective terms. Fixed time step size of 0.0005 sec to 0.00005 sec with second order accuracy in time domain was used requiring 2400–24000 time steps for one cycle. The momentum interpolation method due to Rhie and Chow [22] was used in a collocated grid arrangement which can satisfactorily overcome the problem of pressure oscillation. The technique involves appropriate interpolation of velocity field at the interface of the cell faces. It has been demonstrated that such momentum interpolation is equivalent to solving a continuity equation with an added fourth derivative of pressure which does not change the for-

mal second order accuracy of the basic discretization process. The procedure was also successfully implemented in a previous work by Nandi and Chattopadhyay [23]. In order to check the faithful repetition of result after grid convergence test, a multiple cycle simulation had been carried out for reproducibility of the result, and it has been reported in Fig. 4.

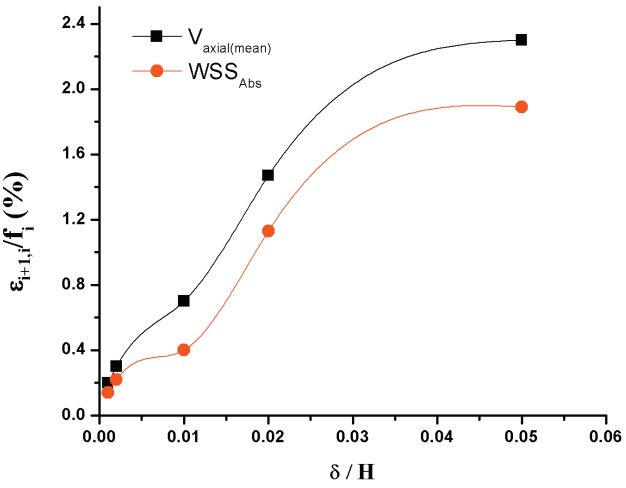

Fig. 3. Comparison of global results normalized by the extrapolated value, between three grid solutions and Richardson extrapolation estimation

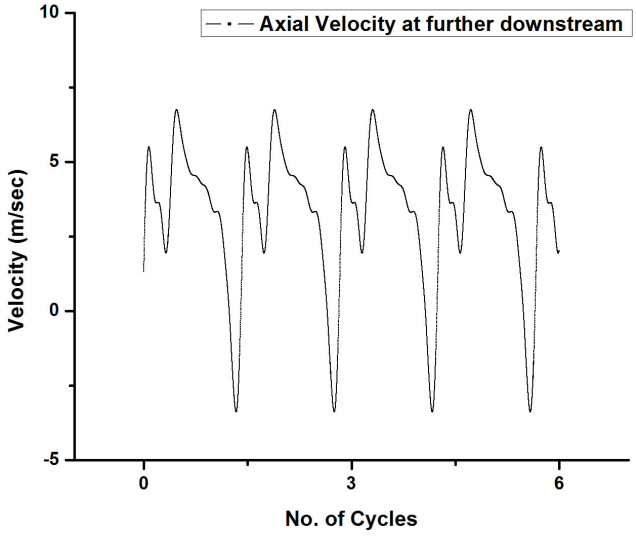

Fig. 4. Repetitive cycle of results reflecting axial velocity profile at near-outlet downstream

3. Results

From the calculated data, important fluid-mechanical parameters of interest such as shear stress, vortical structures, pressure profile and velocity distribution have been evaluated. Two important parameters need special mention in this connection having relevance to the health of arterial tissue [18], namely, the time-averaged wall shear stress (TAWSS) and the oscillatory shear index (OSI). While TAWSS can be simply integrated and averaged over a cycle, OSI is defined as

$$\mathrm{OSI} = \frac{1}{2}\left(1 - \frac{\tau_{\mathrm{mean}}}{\tau_{\mathrm{mag}}}\right) \tag{19}$$

where τ_{mean} is the time-mean wall shear stress and τ_{mag} is the time-mean magnitude of the wall shear stress. OSI has a range between 0 and 0.5, where 0.5 defines purely oscillatory flow. Areas of high OSI would lead to endothelial dysfunction and artherogenesis [18] and hence the detection of such zones is very important.

It is well understood that the flow structure of stenosed vessel is dominated by vortical structures and post-stenotic recirculation region [9]. Figure 5 shows contour plot of time averaged velocity stream function for type 1 inlet velocity profile at different degree of stenoses considering Power Law Viscosity model. Comparison has been made at two different Reynolds numbers (Re I and II) in the figure. At low Reynolds number, recirculation bubbles propagate away from the region of stenoses with time for a lower severity of stenoses of 25%. However, at higher Reynolds number the same severity of stenoses causes complex flow structure with multiple recirculation bubbles moving away from the region of stenoses with time. On increasing the degree of stenoses (to 56%) at low Reynolds number, recirculation bubbles oscillate in axial direction and accumulate to form large eddies with time. Same phenomena occur while increasing the Reynolds number of inlet flow. At 80% stenoses, recirculation bubbles drive inside towards the stenoses with time due to the decrease in pressure shedding at low Reynolds number along downstream with development of flow, and it dissipates into multiple recirculation bubbles forming complex structure with an increase in Reynolds number as found earlier [9].

Figure 6 shows a comparison of OSI at different Reynolds number for two different viscosity models (Power Law and Quemada) at different degree of stenoses. For type 1 inlet velocity profile, both the viscosity models exhibit almost similar nature of OSI curves with peak value of 0.5 at post stenoses region for 25% stenoses. Shifting of the peak value of OSI is also noticed for higher Reynolds number in the case of 56% stenoses, with a significant variation in OSI distribution along the length of the vessel at different *Re*. But at 80% stenoses, type 1 inlet velocity profile yield maximum OSI of 0.2 to 0.25 at the distal end of

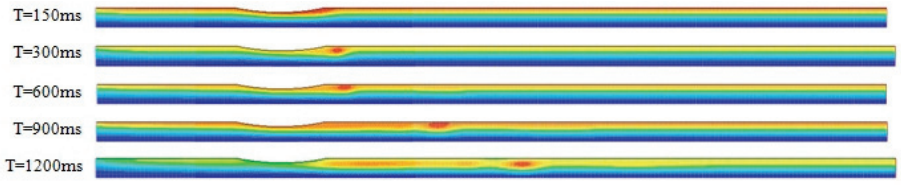

(i) 25% Stenoses: Re I

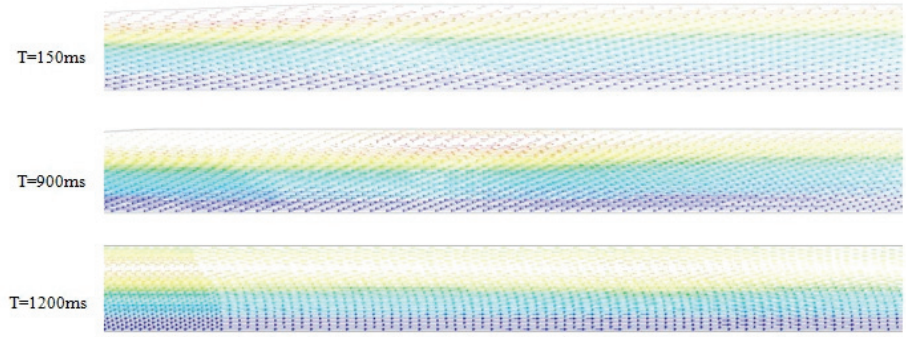

a (i-i) Recirculation region at 25% stenoses: Re I

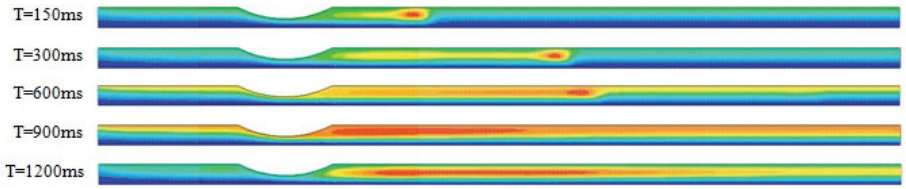

(ii) 56% Stenoses: Re I

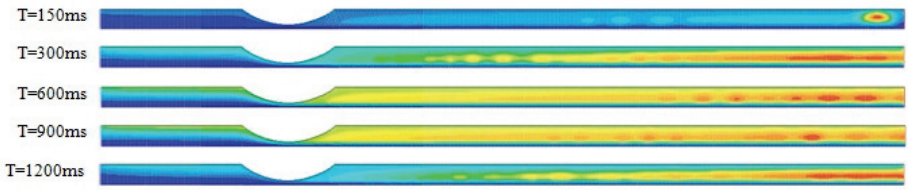

(iii) 80% Stenoses: Re I

(a)

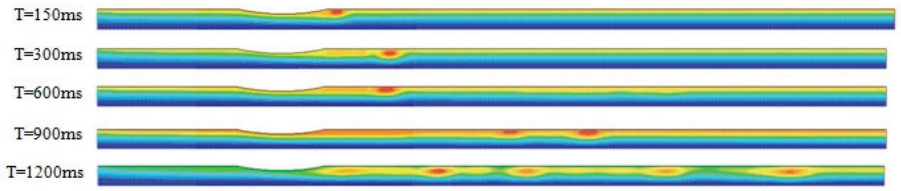

(i) 25% Stenoses: Re II

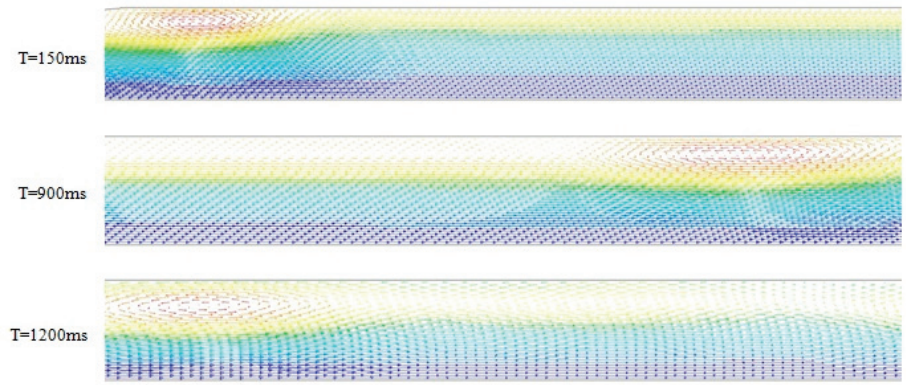

b (i-i) Recirculation region at 25% stenoses: Re II

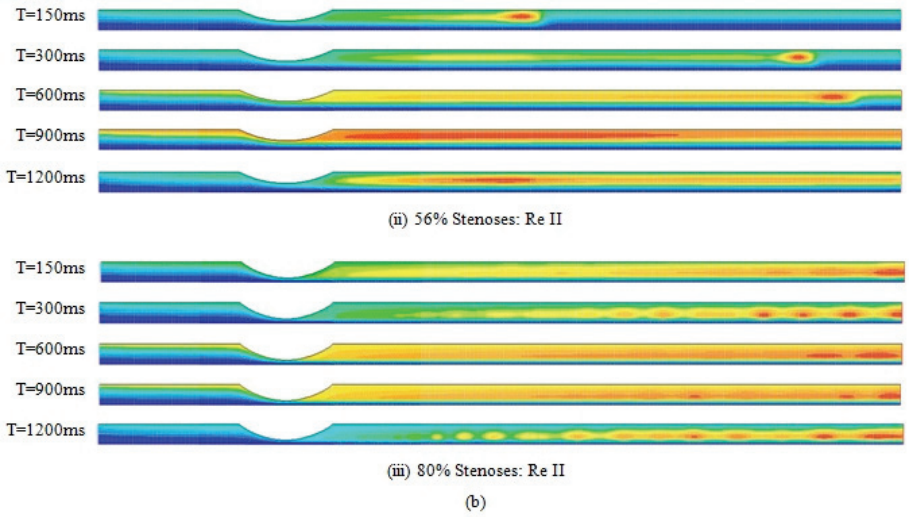

Fig. 5. Time averaged stream function of velocity for Power Law model with Type 1 inlet velocity at different degrees of stenoses (25%, 56% and 80%) at (a) Re I and (b) Re II, with inset of re-circulation zone in 25% stenoses case (i-i) for (a) and (b), respectively

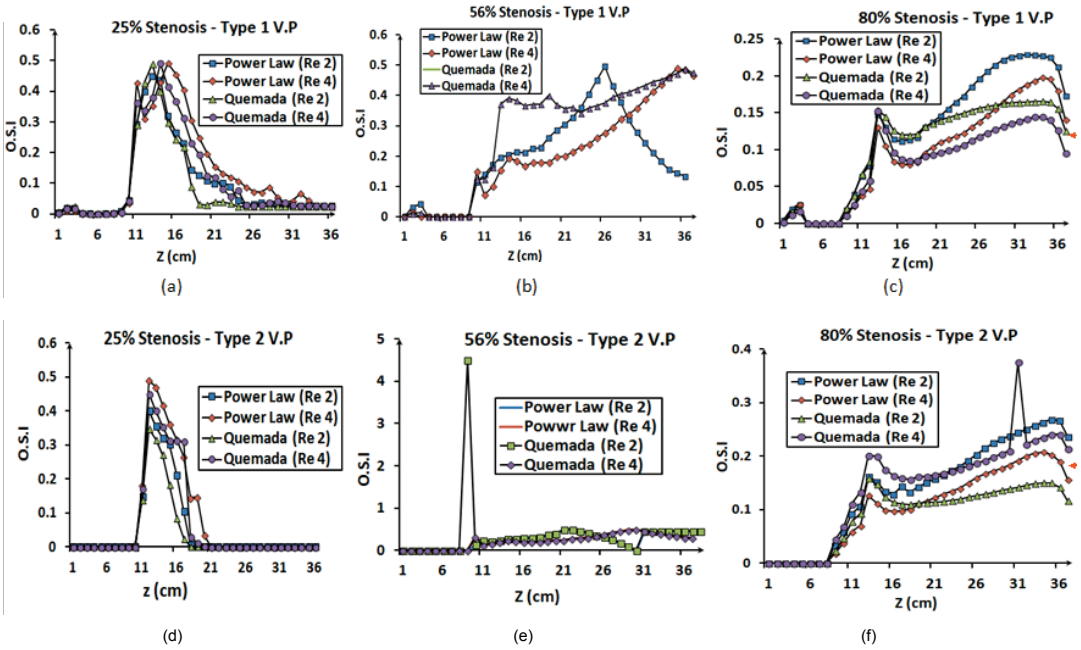

Fig. 6. Comparison of OSI distribution for different viscosity models: (a) Type 1 inlet velocity: 25% stenoses, (b) Type 1 inlet velocity: 56% stenoses, (c) Type 1 inlet velocity: 80% stenoses, (d) Type 2 inlet velocity: 25% stenoses, (e) Type 2 inlet velocity: 56% stenoses, (f) Type 2 inlet velocity: 80% stenoses, (g) Type 3 inlet velocity: 25% stenoses, (h) Type 3 inlet velocity: 56% stenoses, (i) Type 3 inlet velocity: 80% stenoses

the vessel, and the pattern remains almost identical for different Reynolds number at different viscosity models. In the case of type 2 inlet velocity profile, at 25% stenoses both Power Law and Quemada viscosity models exhibit maximum OSI at post stenoses region for both low and high Reynolds number. However, variation in OSI was observed by Tan et al. [18] as their domain of study varies to bifurcation, and inlet boundary condition remains distinct from that of physiological conditions.

In Fig. 7, a comparative study of average shear stress on the wall of the vessel at different degree of stenoses was made for two different Reynolds numbers. It is observed that high shear stress results from flow at higher Reynolds number, as depicted by Siddiqui et al. [12], and the magnitude of the peak of average shear stress increase sharply from 7 to 40 and 500 with the increase in degree of stenoses from 25% to 56% and 80%, respectively. Temporal Wall Shear Stress (WSS) at locations of 2 cm, 9 cm and 18 cm

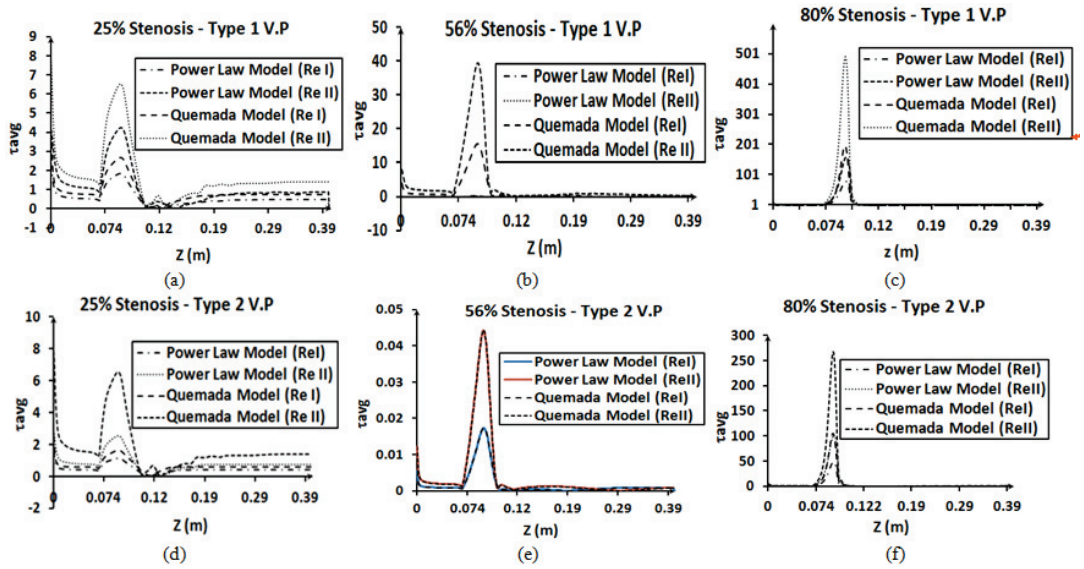

Fig. 7. Effect of Reynolds number on average WSS distribution using type 1 and type 2 inlet velocity at different degree of stenoses for different rheological models (Power Law and Quemada)

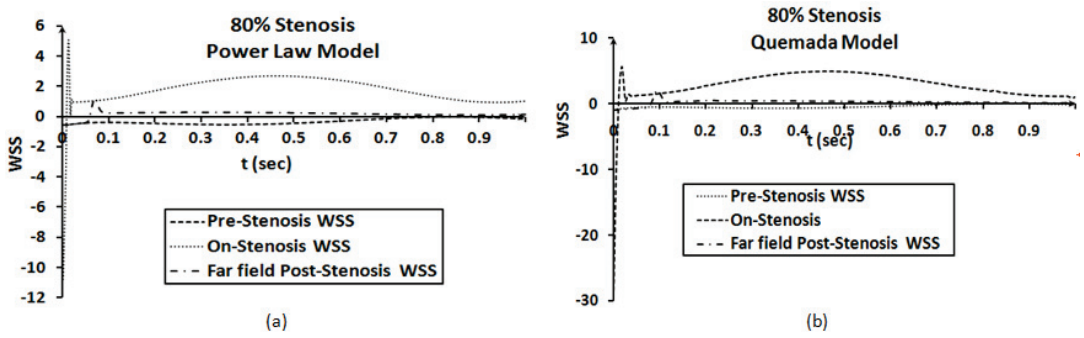

Fig. 8. Temporal WSS for the first cycle (1.0 sec) in the case of 80% Stenoses for (a) Power Law Model and (b) Quemada Model

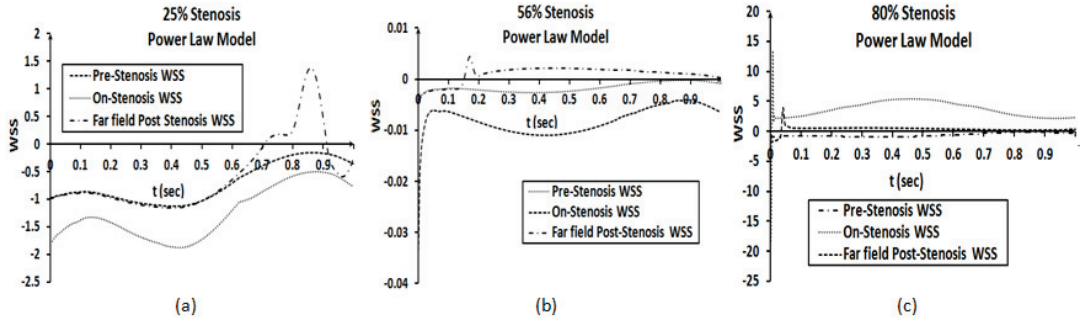

Fig. 9. Temporal WSS plot at different degree of stenoses for type 1 input velocity profiles considering Power Law model at (a) 25% stenoses, (b) 56% stenoses, (c) 80% stenoses

from the inlet (i.e., pre-, on- and post-stenotic zone) along the vessel length has been compared at different length of the vessel for two different viscosity models at 80% stenoses as shown in Fig. 8. It has been observed that WSS in the region of stenoses varies widely while applying Quemada model at the initial stage of flow. While Power Law model shows a negative WSS of –12 initially in the region of stenoses, quite similar to numerical investigation findings by Beratilis et al. [2], and the corresponding for Quemada model is –30. It is also noticed that variation of WSS in the pre-stenoses region for both the models is quite insignificant and very low, thus it can be neglected in further studies.

Temporal WSS variation for three different degrees of stenoses along the wall of the vessel for Power law model is compared in Fig. 9. For type I velocity profile, while at pre-stenoses region WSS varies insignificantly at 80% stenoses, it varies from –1 to –0.25 for 25% stenoses with time, and the variation dampened with the increase in degree of stenoses. A detailed study of axial velocity along the centreline is shown in Fig. 10. Power Law viscosity for blood is considered here with variation in the degree of stenoses from 25–80%. Velocity curve representation at each successive time step of T/8 depicts the resemblance of gradient variation of mean axial velocity about the centreline with that of inlet plug pulsatile velocity profile. The overshoot of temporal velocity in the region of stenoses (0.07 m. –0.116 m) indicates the presence of gradient flow breaker in each type of stenoses. In Fig. 11, it has been shown that magnitude of wall pressure increases both for increase and decrease of stenoses from 50% stenoses (approximately). Physics behind this variation is yet not clear, and it has not been discussed in the literature yet.

4. Discussion

In the of higher Reynolds number, the peak of OSI shifted slightly away from the region of stenoses as compared to the earlier case, because at higher Reynolds number, the dissipation of energy by the fluid at the wall immediately after stenoses reduces dynamic pressure further downstream during higher stress relaxation factor of the corresponding viscoelastic fluid. For both types of inlet velocity profiles, Quemada viscosity model exhibits higher value for average wall shear stress than that of Power Law model. It has been found that the region just immediate after stenoses is prone to very low wall shear stress, irrespective of the flow rate. This is linked to the existence of recirculation pattern at such locations. At high degree of stenoses, post stenoses wall has low value of wall shear stress (about 0.5), development of prone region for re-stenoses at downstream of flow. Development of wall shear stress at post stenoses wall has been found at low degree of stenoses (25%), indicating low susceptibility of re-stenoses at

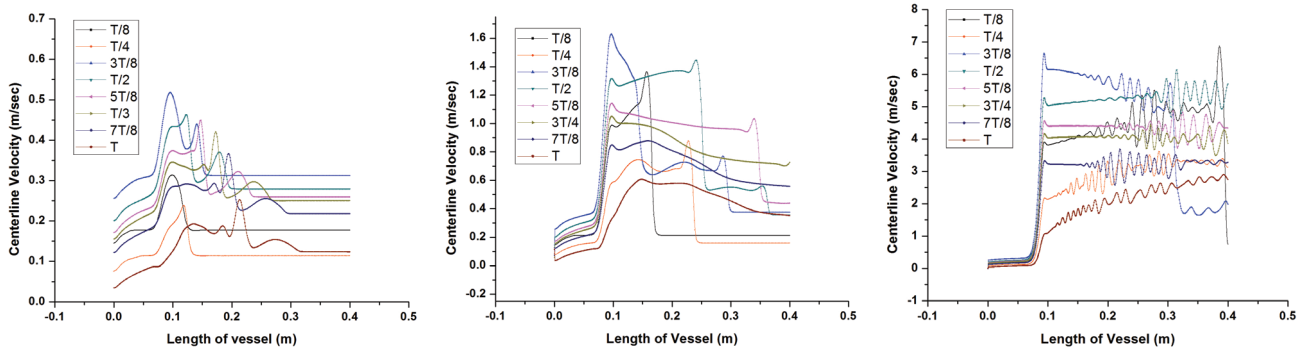

(a) 25% stenoses (b) 56% stenoses (c) 80% stenoses

Fig. 10. Velocity plot at different degree of stenoses for type 2 input velocity profile at each T/8 time steps considering Power Law model

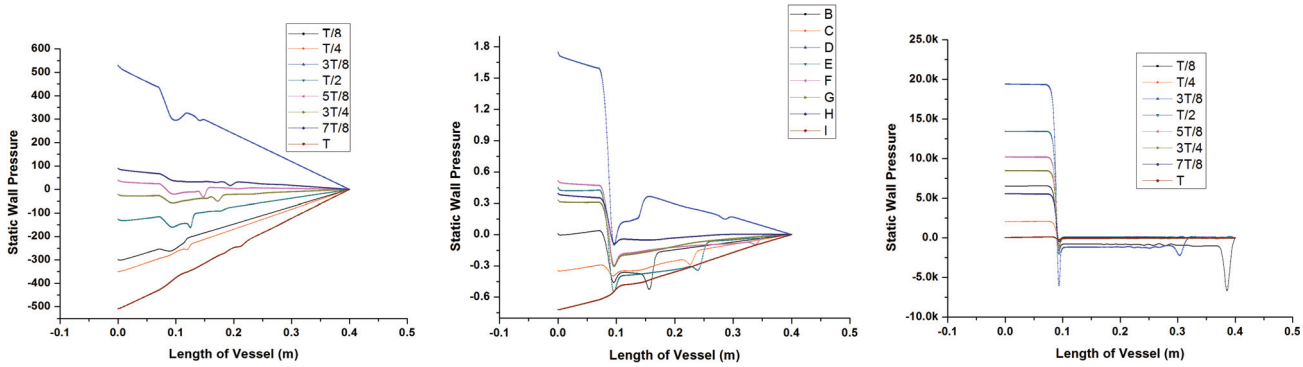

(a) 25% stenoses (b) 56% stenoses (c) 80% stenoses

Fig. 11. Static Wall Pressure plot at different degree of stenoses for type 2 input velocity profile at each T/8 time steps considering Power Law model

further downstream. Re-stenoses can also occurs in vessel with higher degree of blockage due to much higher gradient change in wall sear stress across the region of stenoses, and thus responsible for development of vortices near immediate post stenoses wall. Thus it can be concluded that even at pre-stenoses region flow structure varies widely at the onset of stenoses. It has been observed that WSS oscillates from negative to positive values at the end of the time cycle for 25% stenoses, and for 56% stenoses, it follows a symmetrical pattern.

On comparative study among the degree of stenoses, it has been found that mean axial velocity increases (from 0.3 m/sec to 4.5 m/sec approximately) with an increase in degree of stenoses along the centreline. It indicates flow development from laminar to transition as blockage increases due to the increase in kinetic energy of the flow structure. Thus, it leads to vortex development at further downstream of stenoses due to formation of temporal-spatial low pressure region due to dissipation of energy by the molecules of the fluid in those regions.

Although the spatial and temporal distribution of magnitude of axial velocity increases with increase in Reynolds number by two-fold, yet there are insignificant changes in the pattern of the same, except an occasional overshoot of axial velocity at further downstream at low Reynolds number due to cumulative stress response of the fluid. As the fluid at wall has been considered to be of no-slip boundary condition, static wall pressure has been considered for comparative study of wall pressure at different degree of stenoses. Interestingly negative overshoot of wall pressure has been found at further downstream of stenoses, which increases with an increase in the degree of stenoses, confirming recirculation of flow. Phenomena for recirculation (vortex formation) had already been discussed.

5. Conclusion

The present work combines pulsating flow and non-Newtonian rheology for investigating flow structure in stenosed artery. The location and movement of recirculation bubbles are found to be dependent on the degree of stenoses. At higher blocakge, transient WSS profile shows symmetrical nature for both types of input velocity profiles. As the geometry of blockage induces narrow duct to the flow of the fluid, it leads to the development of laminar to transition flow. Considering the viscosity property of the fluid to be non-Newtonian, especially considering hematocrit component of the fluid (blood) in case of Power Law model and Quemada model, contribution to the steep increase in WSS at downstream of post stenoses region is of significance. While considering hematocrit components of blood, which are macromolecules, flow behavior changing from laminar to transition leads to greater dissipation of energy by these molecules. Dissipation of energy in terms of temporal heat leads to the development of quasi-spatial low pressure region, which drives the phenomena of vortex formation in those regions. Similarly, with the development of vortices, oscillatory nature of WSS decreases, leading to low OSI. And temporal low value of OSI leads to spatial aggregation of macromolecules at the wall, leads to development of re-stenoses at further downstream.

Acknowledgment

HC acknowledges support from PURSE Programme of Department of Science and Technology.

References

[1] AI L., ZHANG L., DAI W., HU C., SHUNG K.K., HSIAI T.K., *Real-time assessment of flow reversal in an eccentric arterial stenotic model*, J. Biomech., 2010, 43, 2678–2683.

[2] BERATILIS N., BALARAS E., PARVINIAN B., KIGER K., *A numerical and experimental investigation of transitional pulsatile flow in a stenosed channel*, J. Biomech. Eng., 2005, 127, 1147–1157.

[3] DRIKAKIS D., MILIONIS C., PAL S.K., SHAPIRO E., *Assesment of the applicability of analytical models for blood flow prediction in reconstructive surgery*, Int. J. Numerical Methods in Biomed. Eng., 2011, 27, 993–999.

[4] IQBAL M.A., *Viscoelastic blood flow through arterial stenoses – Effect of various viscosity*, Int. J. Nonlinear Mech., 2012, 47, 888–894.

[5] JOHNSTON B.M., JOHNSTON P.R., CORNEY S., KILPATRICK D., *NonNewtonian blood flow in human right coronary arteries: steady state simulations*, J. Biomech., 2006, 39, 1116–1128.

[6] JINYOU Y., YANG H., *Numerical simulations of non-Newtonian blood flow in human thoracic aortic dissection based on CT image*, IEEE Trans. of Biomed. Eng., 2011, 978(1), 238–252.

[7] LI Z., KLEINSTREUER C., *Fluid-structure interaction effects on sac-blood pressure and wall stress in a stented aneurysms*, J. Biomech. Eng., 2005, 127, 662–671.

[8] MITTAL R., SIMMONS S.P., UDAYKUMAR H.S., *Application of Large-Eddy-Simulation to the study of pulsatile flow in a modeled arterial stenosis*, J. Biomech. Eng., 2001, 123, 325–332.

[9] NEOFYTOU P., DRIKAKIS D., *Effects of blood models on flow through a stenosis*, Int. J. Num. Methods in Fluid, 2003, 43, 597–635.

[10] OJHA M., *Wall shear stress temporal gradient and anastomotic intimal hyperplasia*, Cir. Research, 1994, 74, 1227–1231.

[11] ROHLF K., TENTI G., *The role of Womersley number in pulsatile blood flow a theoretical study of the Casson model*, J. Biomech., 2001, 34, 141–148.

[12] SIDDIQUI S.U., VERMA M.K., MISHRA S., GUPTA R.S., *Mathematical modeling of pulsatile flow of Casson's fluid in arterial stenosis*, J. Ap. Math. and Com., 2009, 210, 1–10.

[13] TAYLOR C., HUGHES T., ZARINS C., *Finite Element Modeling of Blood Flow in Arteries*, Com. Meth. in Ap. Mech. and Eng., 1998, 158(1–2), 155–196.

[14] WOMERSLEY J.R., *Method for the calculation of velocity, rate of flow and viscous drag in arteries when the pressure gradient is known*, J. Physiol., 1955, 127, 553–563.

[15] WALBURN F.J., SCHNECK D.J., *A constitutive equation for whole human blood*, Biorheology, 1976, 13, 201–219.

[16] KU D.N., GIDDEN D.P., ZARINS C.K., GLAGOV S., *Pulsatile flow and atherosclerosis in the human carotid bifurcation: Positive correlation between plaque and low oscillating shear stress*, Arteriosclerosis, 1985, 5, 293–302.

[17] QUEMADA D., *Rheology of concentrated disperse systems III. General features of the proposed non-newtonian model. Comparison with experimental data*, Rheo. Acta, 1977, 17, 643–653.

[18] TAN F.P.P., SOLOPERTO G., BASHFORD S., WOOD N.B., THOM S., HUGHES A., XU X.Y., *Analysis of flow disturbance in a stenosed carotid artery bifurcation using two-equation transitional and turbulence models*, J. Biomech. Eng., 2008, 130, 1–12.

[19] ROACHE P.J., *Perspective: A method for uniform reporting of grid refinement studies*, J. Fluids Eng., 1994, 116(3), 405–41.

[20] STERN F., WILSON R.V., COLEMAN H.W., PATERSON E.G., *Comprehensive approach to verication and validation of CFD simulations.* Part 1. *Methodology and procedures*, J. Fluids Eng., 2001, 123(4), 793–802.

[21] PATANKAR S.V., *Numerical Heat Transfer and Fluid Flow*, McGraw–Hill, New York 1980.

[22] RHIE C.M., CHOW W.L., *Numerical Study of the Turbulent Flow Past an Airfoil with Trailing Edge Separation*, AIAA J., 1983, 21, 1525–1532.

[23] NANDI T., CHATTOPADHYAY H., *Simultaneously developing flow in microchannels under pulsating inlet flow condition*, Int. J. Transp. Phen., 2012, 13, 110–120.